Multiparameter Adaptive Target Classification Using Full-Polarimetric GPR: A Novel Approach to Landmine Detection

Haoqiu Zhou, *Student Member, IEEE*, Xuan Feng, *Senior Member, IEEE*, Zejun Dong, Cai Liu, and Wenjing Liang

***Abstract*—Full-polarimetric ground penetrating radar (FP-GPR) can measure the ability of an object to change the polarization of electromagnetic waves. Compared to the traditional GPR, it has a stronger capability to identify underground objects. In recent years, a series of polarization decomposition methods have been applied to the FP-GPR data processing to obtain the polarimetric attributes and enhance the capability of targets identification. Different polarimetric attributes characterize different features of a target but there is still no effective way to integrate these attributes and take their respective advantages for target classification. In this article, we propose a particle center AdaBoost (PCAD) method and achieve the multiparameter adaptive target identification. The experimental results indicate that the PCAD method can automatically select suitable parameters during the training process for different targets. Compared to the single-parameter classification and the AdaBoost methods based on the traditional average and Bagging method, the PCAD method presents higher correct rates in classification. Finally, the proposed method is applied to landmine detection. The results demonstrate that the landmine is a composite scatterer that can generate surface scattering signals on its surface and dipole and volume scattering signals from its interior; based on the color-coded two-dimensional image by PCAD, we can distinguish landmines from other targets.**

***Index Terms*—Full-polarimetric ground penetrating radar (FP-GPR), identification, landmine detection, multiparameter.**

I. Introduction

SUBSURFACE target identification is a significant application of ground penetrating radar (GPR). For a long time, imaging is the primary way to identify underground objects for GPR [1]–[3]. The migration method is one of the most mature approaches to return the reflected and diffracted signals to their original positions and reconstruct the subsurface image. The geometric features obtained from the reconstructed image can be applied to the target identifications [3], [4]. However, targets with similar geometric features cannot be identified by the imaging techniques [4]–[6]. Therefore, the full-polarimetric GPR (FP-GPR) has been developed to detect underground objects. The FP-GPR can measure the effects of the induced field rotation (IFR) when the electromagnetic wave irradiate on the targets [7], [8]. These effects are closely related to the shape of targets and can be described using a Sinclair matrix [4]. By analyzing the matrix, many polarimetric attributes beyond the geometric features can be extracted and used for identifications.

In the early time, polarimetric techniques were applied to fracture detection for both the ON-ground GPR and the borehole radar [9]–[12]. Some researchers combined the polarimetric method with full waveform inversion to enhance the fracture-detection capability [13]. On the other hand, the polarimetric methods were also applied to the detection of landmine and unexploded ordnance (UXO) [14]–[17]. These works studied the polarimetric characterization of landmines and UXOs and discussed the effects of the ground surface on polarimetric features [18]. Besides, the polarimetric techniques were also applied to subsurface pipe detection [19], [20]. These impressive works have greatly promoted the development of FP-GPR.

In recent years, the polarimetric decomposition methods originated from polarimetric synthetic aperture radar (SAR) [21] were applied to FP-GPR [4]–[6], [22]. These techniques can extract the polarimetric attributes from FP-GPR data and largely improved the target identification capability of GPR. Here, we introduce three classical decomposition methods for example. H-Alpha decomposition is a classical polarimetric analysis method based on mathematical constructions, which can obtain two parameters, H and α, for classification [4], [23], [24]. Apart from the research of target identification, Dong *et al.* [7] also studied the effects of rough surface on the H-Alpha analysis. Freeman decomposition (FD) is a type of physical model-based decomposition method, which can obtain the power of three basic scattering components [25]. The third method is a scattering similarity based decomposition method [26]. This method can automatically identify the major and minor scattering mechanisms rather than the average scattering mechanism of the classical H-Alpha method [27].

Polarimetric decomposition methods are in development and more theories are proposed. However, these methods are all

Manuscript received December 25, 2021; revised February 10, 2022; accepted March 5, 2022. Date of publication March 15, 2022; date of current version April 6, 2022. This work was supported in part by the Science and Technology on Near-Surface Detection Laboratory, in part by the National Key Research and Development Program of China under Grant 2021YFC1523401, in part by the Technology Innovation Center for Land Engineering and Human Settlements, Shanxi Land Engineering Construction Group Co., Ltd., and Xi'an Jiaotong University under Grant 2021WHZ0080, in part by the Graduate Innovation Fund of Jilin University under Grant 101832020CX226, and in part by the National Natural Science Foundation of China under Grant 41974129. *(Corresponding author: Xuan Feng.)*

The authors are with the College of Geo-Exploration Science and Technology, Jilin University, Changchun 130026, China, also with the Science and Technology on Near-Surface Detection Laboratory, Wuxi 214035, China, and also with the Key Laboratory of Applied Geophysics, Ministry of Natural Resources, Jilin University, Changchun 130026, China (e-mail: zhouhaoqiu_jlu@163.com; fengxuan@jlu.edu.cn; dzj19@mails.jlu.edu.cn; liucai@jlu.edu.cn; 172513381@qq.com).

Digital Object Identifier 10.1109/JSTARS.2022.3159305

based on the theory of SAR. Since some differences of measurement exist between GPR and SAR, such as the medium and distance of propagation for electromagnetic waves, observation methods, and noise characteristics, the polarimetric analysis methods used in SAR may not be suitable for GPR [28]. Therefore, we have proposed a particle center based method [28] before to modified the H-Alpha identification method. Particle center is a type of proposed data center, which is a better representation of the sample with fewer effects of the outliers [28] and can enhance the identification ability of FP-GPR. However, this method is mainly for the double-parameters classification such as the H and α features and has difficulties when it is promoted to multiparameter identification. Since different polarimetric parameters characterize different features of a target and there is still no effective way to integrate these parameters and take their respective advantages for target classification, developing a multiparameter identification method is also an effective way to improve the identification accuracy apart from the modification of algorithms.

We focus on both the multiparameter analysis and the modification of identification methods and have proposed a multiparameter adaptive target identification method for FP-GPR based on a particle center AdaBoost (PCAD) method. AdaBoost is a type of classical ensemble learning algorithm that can obtain a strong classifier using a linear combination of several weak classifiers with different weights [29]. In the iterations, the weights of the weak classifiers are computed one by one and the samples misclassified by the previous weak classifier will be focused on in the iteration of the next weak classifier. Finally, a strong classifier can be constructed whose classification error will be less than or equal to the minimum error of all the weak classifiers. This ensemble learning algorithm is greatly suitable for the multiparameter classification and, in this article, each polarimetric parameter can provide one weak classifier. However, similar to other ensemble learning algorithms, the performance of the AdaBoost method greatly depends on the selection of weak classifiers and is much sensitive to the outliers in the training sample [30]. Therefore, the Bagging method [31], random forest method [32], and the attribute Bagging method [33] were proposed to enhance the selection of weak classifiers. Besides, it was also verified that selecting only some of the weak classifiers may perform better than using all of them so the selective ensemble learning was proposed [33], [34].

In this article, we propose a PCAD method. This method starts with searching for the location of the particle center in a sample. The sum of distances between the particle center and all sample points is adopted as the loss function. By using the particle swarm optimization (PSO) method [35], the minimum of the loss function can be easily solved. Subsequently, the original data can be projected into a new domain by computing the L1 norm of the original dataset and the particle center. In the new domain, the attributes selection and weak classifiers determination for subsequent AdaBoost training can be simultaneously and automatically implemented. Finally, both the new dataset and the weak classifiers are applied to the AdaBoost training to obtain the final strong classifier.

The proposed method has the following advantages.

1) By using the particle center processing, the effects of the outliers in the training samples are greatly decreased.
2) The weak classifiers obtained from the new dataset after particle center processing have higher accuracy, which will lead to the higher accuracy of the final strong classifier.
3) By using the particle center method, the adaptive selections of weak classifiers are achieved.

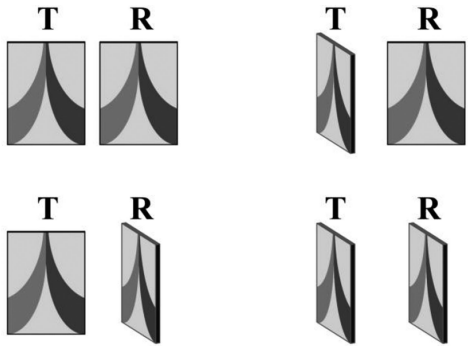

Fig. 1. Four types of antenna combinations of FP-GPR [7].

In general, the proposed PCAD method achieves the multiparameter target identification of FP-GPR, enhances the accuracy of the classical AdaBoost method, and simultaneously solves both the problems of outliers and the automatic selections of weak classifiers. Besides, by comparisons, we prove that the proposed PCAD method is more advanced than the classic Bagging AdaBoost (BAD) method. In the application part, we apply the PCAD method to landmine detection. Based on the PCAD classification results, we generate a color-coded two-dimensional (2-D) image that can present the different scattering mechanisms of the surface and interior of a landmine and help to identify it.

The rest of this article is organized as follows. Section II introduces the polarimetric attributes used in this article. Section III is about the methodology of the proposed PCAD method. In Section IV, the proposed PCAD method is applied to the landmine detection test. Section V discusses the superiority of the proposed method by comparing it with the traditional average and the classic BAD methods. Finally, Section VI concludes this article.

II. Polarimetric Attributes for Identification

A. H-Alpha Attributes

The FP-GPR uses four types of antenna combinations to perform the measurements. The four types of data can construct the Sinclair matrix [S] [21]

$$S = \begin{bmatrix} S_{\mathrm{HH}} & S_{\mathrm{HV}} \\ S_{\mathrm{VH}} & S_{\mathrm{VV}} \end{bmatrix} \tag{1}$$

where H and V represent the horizontal polarization and vertical polarization, respectively. The four components correspond to the collected data using the four types of antenna combinations in Fig. 1.

The scattering vector used in H-Alpha decomposition is defined as [4], [7], [28], [36]

$$k_P = \frac{1}{\sqrt{2}}[\, S_{\mathrm{HH}} + S_{\mathrm{VV}} \;\; S_{\mathrm{HH}} - S_{\mathrm{VV}} \;\; 2S_{\mathrm{HV}} \,]^T. \tag{2}$$

Subsequently, we can obtain a 3 × 3 coherency matrix [*T*] and its singular value decomposition form [7], [21], [23]

$$[T] = k_P \cdot {k_P}^* = \sum_{i=1}^{3} \lambda_i e_i e_i^T \tag{3}$$

$$e_i = \left[\cos\alpha_i \ \sin\alpha_i \cos\beta_i e^{j\delta_i} \ \sin\alpha_i \sin\beta_i e^{j\gamma_i}\right]^T \tag{4}$$

where the symbol* denotes conjugate transpose and λ_i and e_i represent eigenvalues and eigenvectors, respectively, $i = 1, 2, 3$. The α_i, β_i, δ_i, and γ_i are the parameters of the dominant scattering mechanism and are made to enable a probabilistic interpretation of the scattering process. The pseudo probability is defined as $p_i = \lambda_i/(\lambda_1+\lambda_2+\lambda_3)$ [7]. Furthermore, the average scattering angle α and the polarimetric entropy H can be calculated as follows [37]:

$$\overline{\alpha} = \sum_{i=1}^{3} p_i \alpha_i \tag{5}$$

$$H = -\sum_{i=1}^{3} p_i \log_3 p_i. \tag{6}$$

The entropy *H* is a measure of randomness of scattering mechanisms, and the angle α characterizes the scattering mechanism [23], [24].

B. Freeman Attributes

FD is a type of physical model-based, three-component decomposition method [25]. The scattering vector used in FD is defined as

$$k_L = \left[S_{\rm HH} \ \sqrt{2}S_{\rm HV} \ S_{\rm VV}\right]^T. \tag{7}$$

Subsequently, we can obtain a 3 × 3 covariance matrix [*C*] [5], [22], [25], [38]

$$[C] = k_L \cdot k_L^* = \begin{bmatrix} |S_{\rm HH}|^2 & \sqrt{2}S_{\rm HH}S_{\rm HV}^* & S_{\rm HH}S_{\rm VV}^* \\ \sqrt{2}S_{\rm HV}S_{\rm HH}^* & 2|S_{\rm HV}|^2 & \sqrt{2}S_{\rm HV}S_{\rm VV}^* \\ S_{\rm VV}S_{\rm HH}^* & \sqrt{2}S_{\rm VV}S_{\rm HV}^* & |S_{\rm VV}|^2 \end{bmatrix}. \tag{8}$$

The [*C*] is considered to be composed of three matrices, which can be represented as follows [5], [22], [25], [38]:

$$\begin{aligned}[C] &= [C_s] + [C_d] + [C_v] \\ &= f_s \begin{bmatrix} |b|^2 & 0 & b \\ 0 & 0 & 0 \\ b^* & 0 & 1 \end{bmatrix} + f_d \begin{bmatrix} |a|^2 & 0 & a \\ 0 & 0 & 0 \\ a^* & 0 & 1 \end{bmatrix} + \frac{f_v}{8} \begin{bmatrix} 3 & 0 & 1 \\ 0 & 2 & 0 \\ 1 & 0 & 3 \end{bmatrix} \\ &= \begin{bmatrix} f_s|b|^2 + f_d|a|^2 + \frac{3f_v}{8} & 0 & f_s b + f_d a + \frac{f_v}{8} \\ 0 & \frac{2f_v}{8} & 0 \\ f_s b^* + f_d a^* + \frac{f_v}{8} & 0 & f_s + f_d + \frac{3f_v}{8} \end{bmatrix} \end{aligned} \tag{9}$$

where $[C_s]$, $[C_d]$, and $[C_v]$ correspond to the covariance matrices of the surface-like scattering, the double-bounce scattering, and the volume scattering, respectively [5]. f_s, f_d, and f_v denote the energy of the $S_{\rm VV}$ signals for the three types of scatterings, respectively. Besides, *a* and *b* represent the data of $S_{\rm HH}/S_{\rm VV}$ for the double-bounce scattering and the surface scattering, respectively [25]. Combining (8) and (9), we can obtain an equation set, which is given by [5]

$$\begin{cases} f_s|b|^2 + f_d|a|^2 + \frac{3f_v}{8} = |S_{\rm HH}|^2 \\ f_s b + f_d a + \frac{3f_v}{8} = S_{\rm HH} \cdot S_{\rm VV}^* \\ f_s + f_d + \frac{f_v}{8} = |S_{\rm VV}|^2 \\ \frac{f_v}{8} = |S_{\rm HV}|^2. \end{cases} \tag{10}$$

By solving the equation set, *a*, *b*, f_s, f_d, and f_v can be obtained. Subsequently, the power of three types of scattering can be derived [5], [38]

$$\begin{cases} P_s = f_s\left(1 + b^2\right) \\ P_d = f_d\left(1 + a^2\right) \\ P_v = f_v. \end{cases} \tag{11}$$

The P_S, P_D, and P_V are the Freeman attributes used in our method.

C. Polarimetric Similarity Attributes

The polarimetric similarity attributes are based on the scattering vector in (2) and the coherency matrix [*T*] in (3), which is given by [26], [27]

$$rs = \frac{k_P^* \left[T\right] k_P}{\text{trace}\left(k_P \cdot k_P^*\right) \times \text{trace}\left([T]\right)} \tag{12}$$

where k_p is the Pauli scattering vector of a canonical scatterer, [*T*] represents the coherency matrix computed using the FP-GPR data of a measured scatterer, trace(·) denotes the trace operation of a matrix [27], and *rs* characterizes the similarity between the canonical scatterer and the measured scatterer [27].

Considering three canonical scatterers, i.e., a surface-like scatterer, a double-bounce scatterer, and a volume scatterer, their Pauli scattering vectors are given by

$$\begin{cases} k_{Ps} = \left[\sqrt{2}\ 0\ 0\right] \\ k_{Pd} = \left[0\ \sqrt{2}\ 0\right] \\ k_{Pv} = \left[0\ 0\ \sqrt{2}\right]. \end{cases} \tag{13}$$

Since the three vectors in (13) are mutually orthogonal, the corresponding similarity attributes, i.e., rs_s, rs_d, and rs_v, satisfy [27]

$$rs_s + rs_d + rs_v = 1. \tag{14}$$

The rs_s, rs_d, and rs_v are the polarimetric similarity attributes used in our method.

III. PCAD Method

A. Construction of Strong Classifier in PCAD Method

Based on Section II, we can obtain eight polarimetric attributes dataset, which can be represented as follows:

$$D = \left[H, \alpha, P_s, P_d, P_v, rs_s, rs_d, rs_v\right]. \tag{15}$$

The first step is to compute the particle center of *D* using the PSO iteration method. The key idea is to use sufficient particles to represent the random solutions. We first suppose the coordinate and velocity of *m*th particle at *i*th iteration

$$\begin{cases} x_m^i = \left(x_{m1}^i, x_{m2}^i, \ldots, x_{m8}^i\right) \\ v_m^i = \left(v_{m1}^i, v_{m2}^i, \ldots, v_{m8}^i\right) \end{cases} \tag{16}$$

where *x* and *v* represent the position and velocity of a particle, which are 8-D corresponding to the eight attributes in (15).

The initialization of (16) uses the normally distributed random numbers.

The sum of distances between the particles in (16) and all sample points in (15) is adopted as the loss function

$$\text{Fit}(x_m^i) = \sum_{n=1}^{N} \sqrt{\sum_{j=1}^{8} \left(x_{mj}^i - D_{nj}\right)^2} \tag{17}$$

where *j* represents the dimension of the particles in (16) and *N* is the number of samples in (15). During the iterations, the value of Fit for each particle is computed. At *i*th iteration, we can obtain the minimum Fit of each particle from 1th to *i*th iterations and the position with the minimum Fit is represented using X_m^i

$$\begin{cases} X_m^i = \arg\min \text{Fit}(x_m) \\ x_m = x_m^1, x_m^2, \ldots, x_m^i. \end{cases} \tag{18}$$

Simultaneously, we can also obtain the minimum Fit of all particles from 1th to *i*th iterations and the position with the minimum Fit is represented using PC^i

$$\begin{cases} \text{PC}^i = \arg\min Fit(X^i) \\ X^i = X_1^i, X_2^i, \ldots, X_m^i. \end{cases} \tag{19}$$

At each iteration, X_m^i and PC^i are obtained and substituted into the following formulas to renew the positions and velocities of particles and finally solve the minimum of (17):

$$\begin{cases} v_m^{i+1} = wv_m^i + c_1 r_1 \left(X_m^i - x_m^i\right) + c_2 r_2 \left(PC^i - x_m^i\right) \\ x_m^{i+1} = x_m^i + v_m^{i+1} \end{cases} \tag{20}$$

where *w* is the inertia weight, r_1, r_2 are two random numbers between 0 to 1, and c_1, c_2 are learning factors [28]. The iteration continues till the variation of PC is less than a threshold μ

$$\sum_{j=1}^{8} \left\|\text{PC}_j^i - \text{PC}_j^{i-1}\right\| \le \mu. \tag{21}$$

When the function converges, PC is the particle center we need and a new dataset can be generated using the L1 norm of the original dataset in (15) and the particle center PC

$$Z = |D - \text{PC}|. \tag{22}$$

Subsequently, every point in *Z* is assigned to a sample weight and the original sample weights are the average values, which is given by

$$\eta_k = (\omega_{k1}, \omega_{k2}, \ldots, \omega_{kN}) = \left(\frac{1}{N}, \ldots, \frac{1}{N}\right)\Big|_{k=1} \tag{23}$$

where ω, *k*, and *N* represent the sample weight, the iteration time, and the number of the training sample, respectively.

In this article, the maximum of *k* is eight, since we use eight attributes. At each iteration, the error of the weak classifier is computed as follows:

$$e_k = \sum_{n=1}^{N} \omega_{kn} \cdot \text{sign}\left(1 - y_n h_k\left(Z_n\right)\right) \tag{24}$$

where h_k represents the weak classifier in the *k*th iteration, $h_k(Z_n) = \{-1, +1\}$, Z_n denotes the *n*th sample in (22), $y_n = \{-1, +1\}$ is the label of the training sample and is known in advance, and –1 and +1 represent the true and false about whether a sample belongs to the class.

According to the error e_k, the weight of *k*th weak classifier can be derived, which is given by

$$\beta_k = \frac{1}{2} \ln\left(\frac{1 - e_k}{e_k}\right). \tag{25}$$

Simultaneously, according to whether a sample is correctly classified ($y_n h_k(Z_n) = 1$) or wrongly classified ($y_n h_k(Z_n) = -1$), the sample weight in (23) can be renewed as follows:

$$\begin{cases} \eta_{k+1} = \frac{\eta_k}{2(1-e_k)} & y_n h_k\left(Z_n\right) = 1 \\ \eta_{k+1} = \frac{\eta_k}{2e_k} & y_n h_k\left(Z_n\right) = -1. \end{cases} \tag{26}$$

Finally, combining the weak classifiers h_k, the weight β_k, and the particle center PC, the presentation of the strong classifier in the PCAD method is given by

$$\text{PCAD}\left(D_{\text{new}}\right) = \sum_{k=1}^{N_k} \beta_k \cdot h_k\left(|D_{\text{new}} - \text{PC}|\right) \tag{27}$$

where N_k is the number of h_k. For a new dataset D_{new}, which is waiting for identification, the identification accuracy can be directly obtained by (27).

B. Simultaneous and Automatic Selection and Determination of Weak Classifiers in PCAD method.

Formula (27) indicates that, apart from PC, another key of the PCAD method is the weak classifiers h_k. As (26) shows, when $e_k < 0.5$, for a correctly classified sample, its weight will decrease in the next iteration, and for a wrongly classified sample, its weight will increase in the next iteration. It means that the samples misclassified by the previous weak classifier will be focused on in the iteration of the next weak classifier. However, if $e_k > 0.5$, which means the weak classifier can not improve the quality of classification results, the weights of the wrongly classified samples will decrease whereas the weights of the correctly classified samples will increase. In this case, the iteration will be time-consuming and unstable and the identification accuracy of the obtained strong classifier will be affected. Therefore, it is important to determine the best weak classifiers and select only some of the attributes that have better performance. It is usually difficult to simultaneously implement the automatic determination and selection of weak classifiers. However, the proposed PCAD method can easily solve the problem after the projection of (22).

Fig. 2 illustrates two examples of the determination and selection of weak classifiers for two attributes. The histograms with four colors are the data samples of four types of targets generated by (22). To identify the blue target, we change the radius of the classifier (see the *x* coordinates in Fig. 2) and compute the error curves, which are given by

$$E_k(r) = \frac{\sum_{n_1=1}^{N_1} \text{sign}\left(Z_{n_1}^1 - r\right) + \sum_{t=2}^{4} \sum_{n_t=1}^{N_t} \text{sign}\left(r - Z_{n_t}^t\right)}{\sum_{t=1}^{4} N_t} \tag{28}$$

where Z^1–Z^4 represent the data of blue, orange, yellow, and purple targets in Fig. 2, respectively, *r* denotes the radius of the weak classifier, and N_t represents the number of samples in Z^t. The red curve in Fig. 2 shows the relation between the error rate and the radius. The optimal weak classifier can be determined

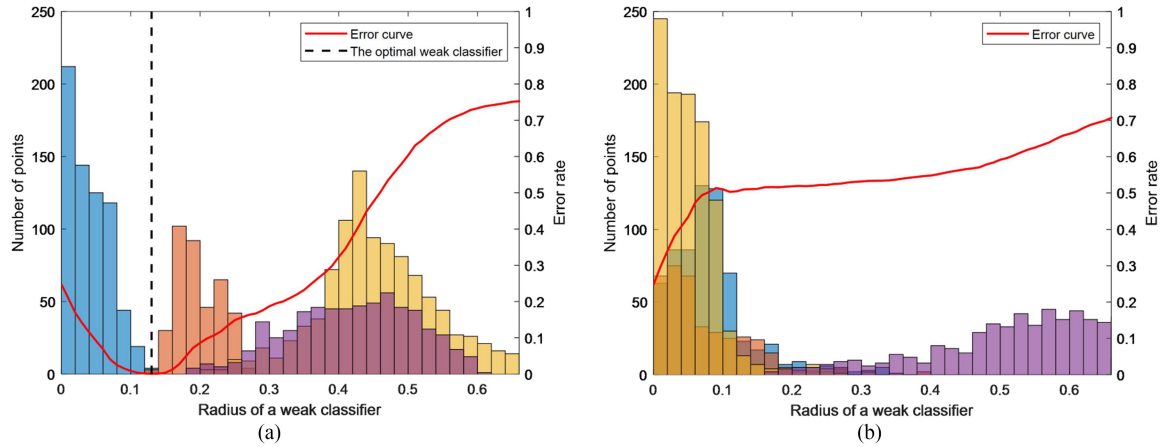

Fig. 2. Examples of the determination of a weak classifier for a parameter. The four color represent four datasets and the dataset with blue color is the set to be classified by the weak classifier. (a) Example of included attribute and weak calssifier. (b) Example of excluded attribute.

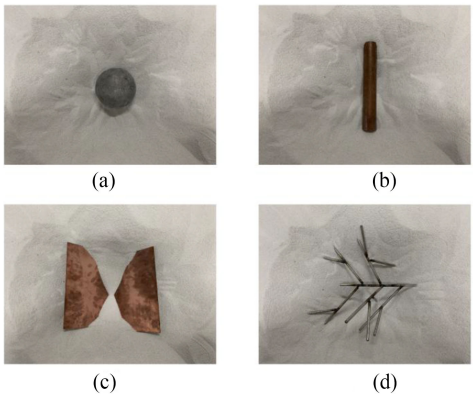

Fig. 3. Four typical targets used in the experiment. (a) Metallic sphere. (b) Metallic cylinder. (c) Metallic dihedral. (d) Metallic multibranch scatterer.

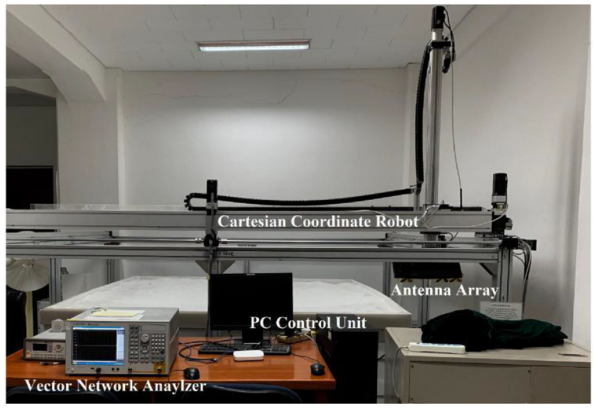

Fig. 4. Stepped frequency ultrawide-bandwidth FP-GPR system.

as follows:

$$h_k(Z) = \begin{cases} 1 & Z \le \arg\min E_k(r) \\ -1 & Z > \arg\min E_k(r) \end{cases}. \tag{29}$$

The dashed line in Fig. 2(a) indicates the radius with minimum error, which is the optimal weak classifier for the parameter. However, the minimum of the error curve in Fig. 2(b) is at $r = 0$ and no weak classifier can be determined. Therefore, the attribute of Fig. 2(b) is not proper for identifying the blue target and will be excluded in the subsequent computation. In general, the attributes selection process can be represented as follows:

$$\begin{cases} \text{Included} & \arg\min E_k(r) > 0 \\ \text{Excluded} & \arg\min E_k(r) = 0 \end{cases}. \tag{30}$$

IV. Implementation

A. FP-GPR Data Acquisition

The FP-GPR data of four typical targets shown in Fig. 3 are collected in the laboratory. The four targets are a metallic sphere, corresponding to the surface-like scatterer; a metallic cylinder, corresponding to the linear scatterer; a metallic dihedral, corresponding to the double-bounce scatterer; and a metallic multibranch scatterer, corresponding to the volume scatterer. The four targets are immersed in a dry sand trough. The experiment uses a stepped frequency ultrawide-bandwidth FP-GPR system (see Fig. 4). The frequency band used in the measurement is 800–4000 MHz. The antenna array is as Fig. 1 shows. The obtained FP-GPR data are shown in Fig. 5. Subsequently, by performing the H-Alpha, Freeman, and polarimetric similarity decomposition, we extract eight polarimetric parameters for the data of four typical targets, which are shown in Fig. 6. The α values are normalized by dividing by 90, as the theoretical α is within 0–90.

B. PCAD Processing Results

The first step is to obtain the particle center of the eight-dimensional datasets in Fig. 6. Here, we present the process of convergence in particle center computations in Fig. 7 to better illustrate the operation of the PCAD method. To clearly observe the process, Fig. 7 only shows two dimensions of the data. The points with four colors are the particles for representing random solutions of particle centers for four datasets of different classes. Fig. 7(a) shows the initialized positions of particles generated by

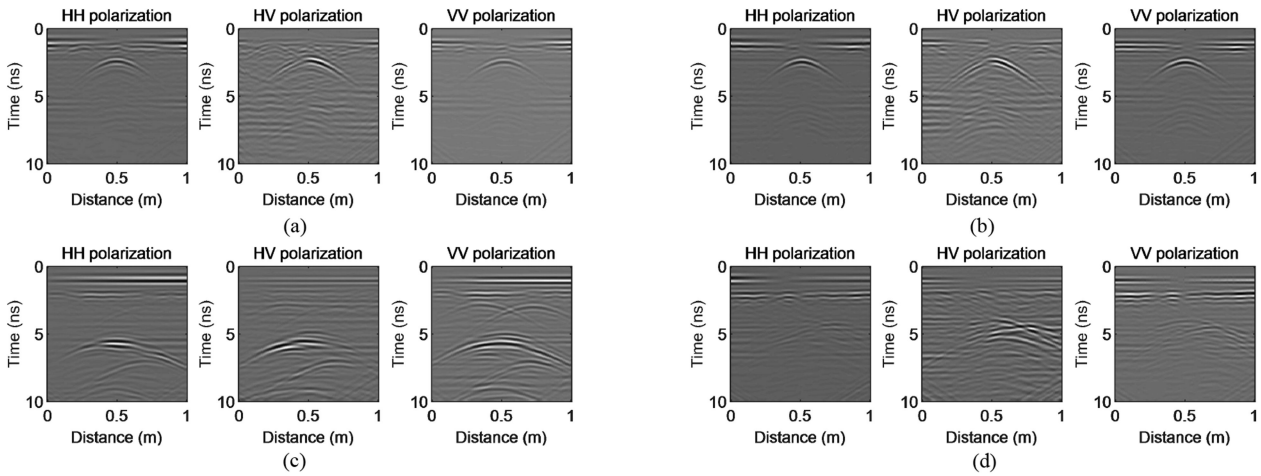

Fig. 5. FP-GPR data of the four typical targets. (a) Metallic sphere. (b) Metallic cylinder. (c) Metallic dihedral. (d) Metallic multibranchscatterer.

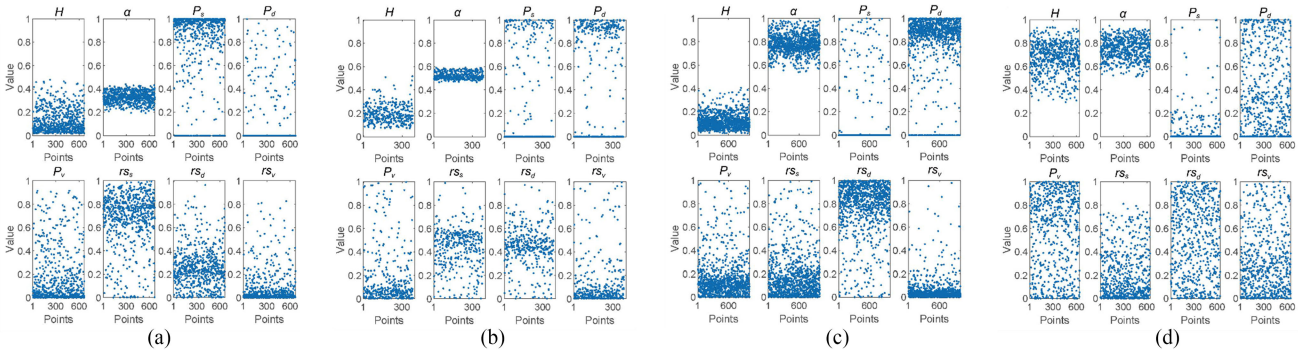

Fig. 6. Extracted eight polarimetric parameters for the data of four typical targets. (a) Metallic sphere. (b) Metallic cylinder. (c) Metallic dihedral. (d) Metallic multibranch scatterer. The α values are normalized by dividing by 90, as the theoretical α is within 0–90.

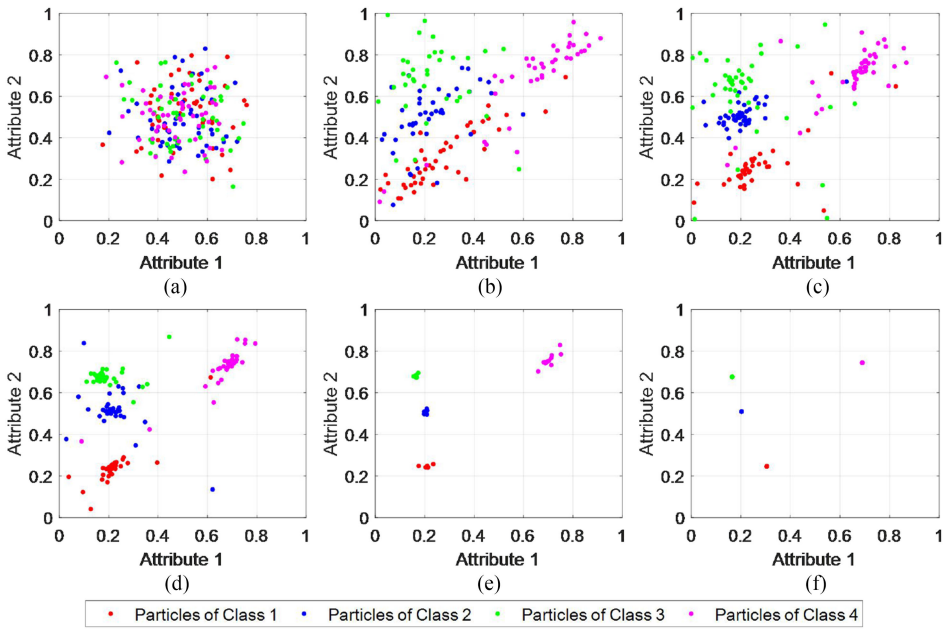

Fig. 7. Process of convergence in particle center computations shown by two dimension of the datasets in Fig. 6. (a) Initialized positions of particles generated by normally distributed random numbers. (b)–(f) Positions of particles after 5, 10, 20, 50, 100 times iteration, respectively.

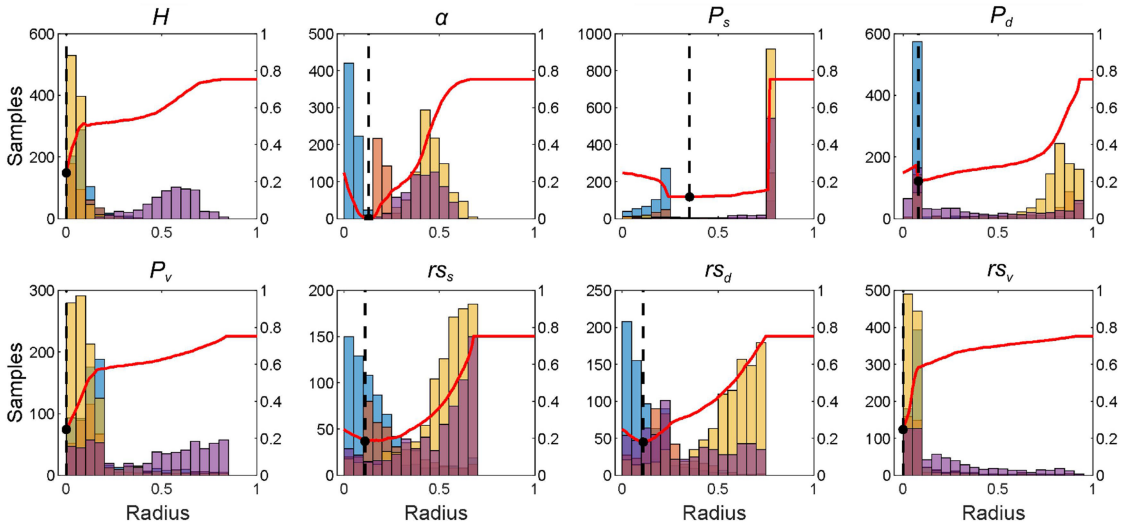

Fig. 8. Determination of weak classifiers for the data of the sphere based on particle center method.

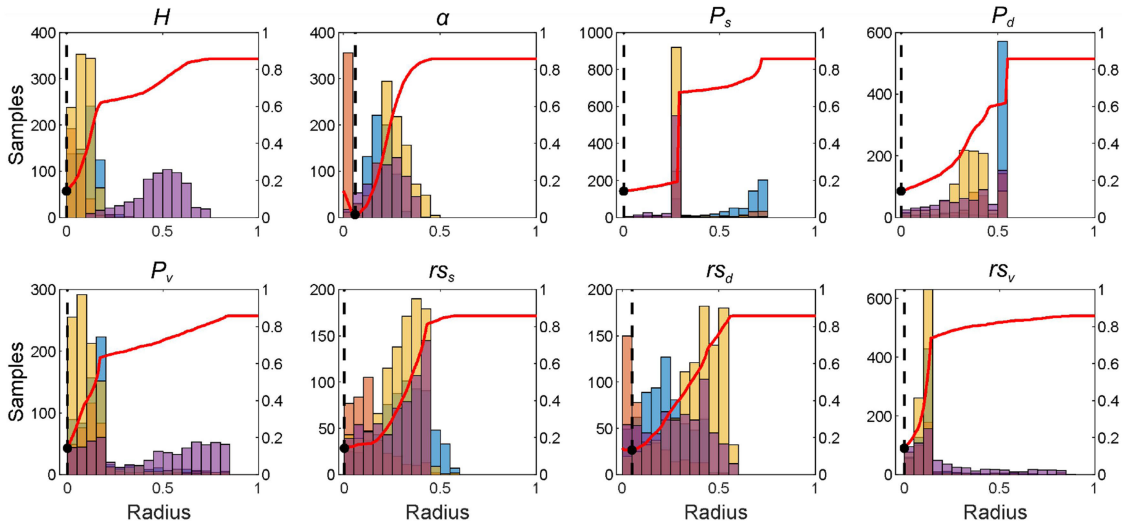

Fig. 9. Determination of weak classifiers for the data of the cylinder based on particle center method.

normally distributed random numbers and Fig. 7(b)–(f) presents the positions of particles after 5, 10, 20, 50, 100 times iteration, respectively. The results clearly show that, as the computation proceeds, the particles of four classes gradually converge at four points. These four points are right the particle centers we need and can be used to project the original data to the new domain.

Subsequently, we analyze the eight polarimetric attributes in detail, respectively, and perform the weak classifiers determinations. Figs. 8–11 presents the analysis for the sphere, cylinder, dihedral, and multibranch scatterer, respectively. Similar to Fig. 2, the histograms in Figs. 8–11 show the distributions of the samples relative to the particle centers. The blue, orange, yellow, and purple histograms correspond to the statistics of the sphere, cylinder, dihedral, and multibranch scatterer, respectively. The red curves indicate the error curves computed using (19); the black points and the black lines represent the minimums of the error curves and the optimal radius of the weak classifiers, respectively.

Fig. 8 aims to identify the data of sphere targets, i.e., the blue histogram. The error curves of parameters H, P_v, and rs_v are monotonically increasing and the minimums of the error curves appear at the position of radius $= 0$. In these cases, the weak classifiers are nonexistent. Therefore, the parameters α, P_s, P_d, rs_s, and rs_d have better performance when identifying the sphere targets. Besides, the minimums of the errors for the parameters α, P_s, P_d, rs_s, and rs_d are all less than 0.5, which correspond to the requirements for weak classifiers discussed in Section III-B. Similarly, the parameters α and rs_d are selected for the cylinder target; the parameters H, α, P_d, P_v, rs_s, rs_d, and rs_v are selected for the dihedral target; the parameters H, P_d, P_v, and rs_v are selected for the multibranch scatterer.

Table I summarizes the attributes selection results, the single parameter identification accuracy, and the multiparameter identification accuracy using the AdaBoost method. For each target, the accuracy after AdaBoost is greater than the accuracy of single parameters. For the targets of the sphere, cylinder,

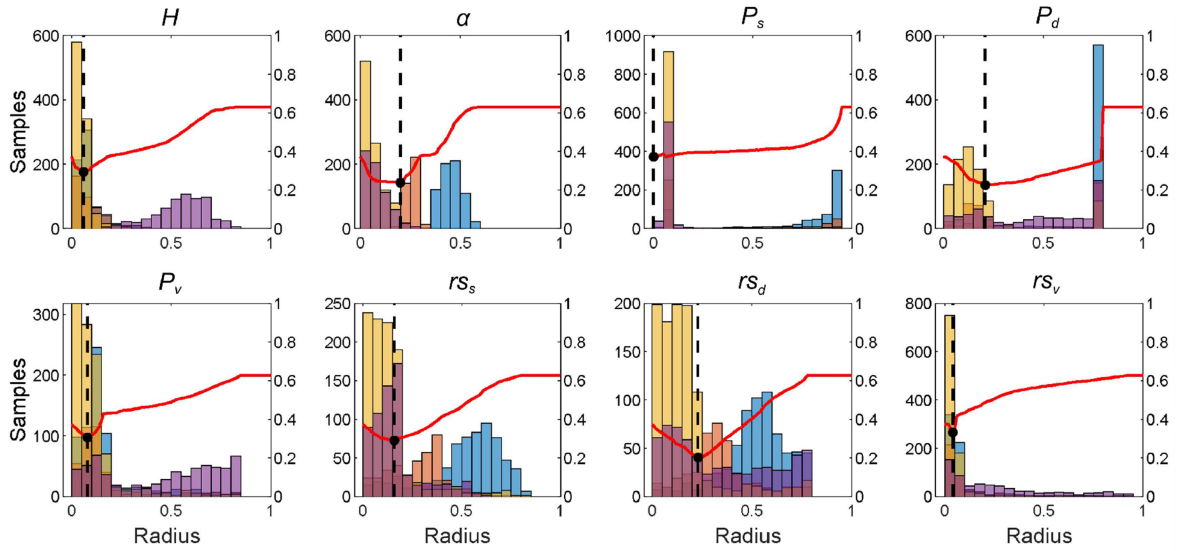

Fig. 10. Determination of weak classifiers for the data of the dihedral based on particle center method.

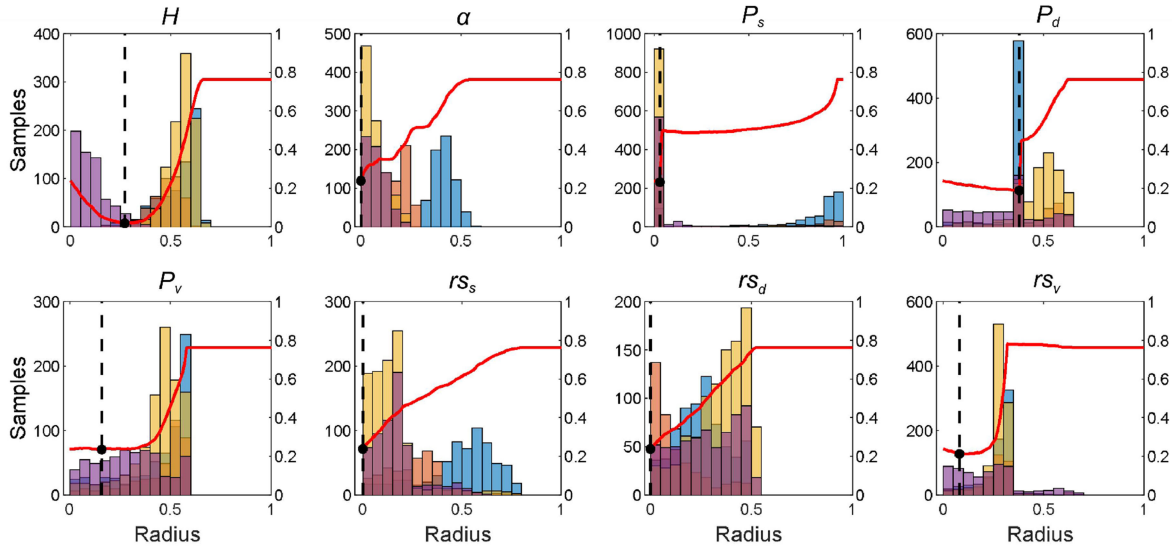

Fig. 11. Determination of weak classifiers for the data of the multibranch scatterer based on particle center method.

and multibranch scatterer, the accuracies of single classifiers are excellent enough, so that the boosts of the AdBoost method are much low. However, for the dihedral target, the single parameter accuracies are approximately about 60% and 70% whereas the multiple parameter accuracy reaches 87.88%. This result verifies that the combination of weak classifiers can indeed promote identification accuracy.

C. Application in Landmine Detection

In this section, the well-trained PCAD classifier is applied to landmine detection. Fig. 12(a) presents the type-72 plastic antitank landmine used for data acquisition and Fig. 12(b) and (c) shows the obtained FP-GPR data before and after Kirchhoff migration, respectively. The migration processing is adopted aiming to improve the quality of imaging. The length of the surveying line and distance interval are 0.7 m and 0.01 m, respectively; the time window and the number of sampling points are 5 ns and 512, respectively; the radar frequencies are from 800 to 4000 MHz.

It is distinct that, in the three radargrams of different polarization modes, the positions of the maximums of the signals from the landmine are different in arriving time. We extract three A-scan signals, which are marked with blue lines in Fig. 12(c) and show them in Fig. 13. The signals from the landmine are circled with red rectangles [see Fig. 12(c)], which can be further divided into two regions (see Fig. 13). The maximums of the signals from the landmine are within region 1 for the HH and VV radargrams but within region 2 for the HV radargram. In region 1, the amplitude of HV signals are far weaker than those of HH and VV signals, which can be interpreted to be the signals from the surface of the landmine; in region 2, the amplitudes

TABLE I
SELECTION OF POLARIMETRIC ATTRIBUTES AND ACCURACY COMPARISONS

Target	Selected polarimetric attributes	Single-parameter accuracy of particle center method (%)	Single-parameter accuracy of average method (%)	Multi-parameter accuracy of particle center method (%)	Multi-parameter accuracy of average method (%)
Sphere (Surface scattering)	α	98.84	98.65	99.93	98.76
	P_s	88.25	88.25		
	P_d	79.74	78.96		
	rs_s	81.56	80.82		
	rs_d	82.04	81.90		
Cylinder (Dipole scattering)	α	97.65	96.40	98.36	97.95
	rs_d	86.73	86.65		
Dihedral (Double-bounce scattering)	H	70.67	70.71	87.88	86.39
	α	76.25	76.25		
	P_d	77.43	76.83		
	P_v	69.33	68.47		
	rs_s	71.00	71.23		
	rs_d	79.85	77.52		
	rs_v	66.80	66.03		
Multibranch scatterer (Volume scattering)	H	97.45	97.18	98.22	98.08
	P_d	76.88	76.81		
	P_v	76.47	76.28		
	rs_v	78.85	78.70		

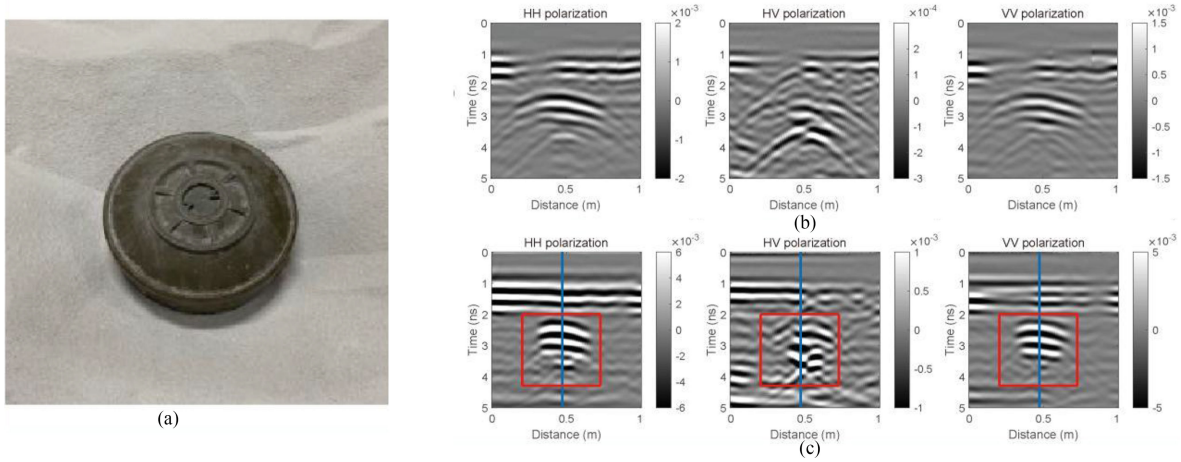

Fig. 12. Application of PCAD in landmine detection. (a) Type-72 antitank landmine used for data acquisition. (b) and (c) Obtained FP-GPR data before and after Kirchhoff migration, respectively.

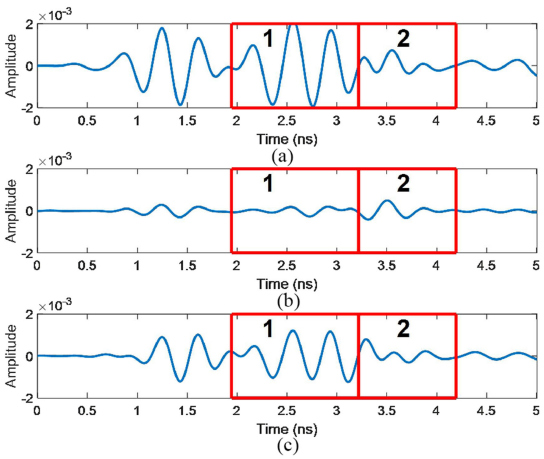

Fig. 13. Extracted signals whose positions are marked with blue lines in Fig. 12(c). Red rectangles correspond to those in Fig. 12(c). (a) HH polarization. (b) HV polarization. (c) VV polarization.

of the signals of three polarization modes are similar and the volume scattering may dominate in this region, which can be interpreted to be the signals from the interior of the landmine. Similar to the metallic multibranch scatterer in Fig. 3(d), the complex structure in the landmine will generate the IFR effects and will increase the amplitude of the cross-polarisation signals.

Subsequently, we applied the well-trained PCAD classifier to the processing of the data in the red rectangles in Fig. 12(c), which means the data contain both region 1 and region 2. The PCAD classification results are shown in Table II, which demonstrate that the signals from the landmine mainly contain surface (71.33%), volume (32.81%), and dipole (18.31%) scatterings and the surface scattering dominates. Since we have observed that the polarization components of the radar data are different in regions 1 and 2, we further obtain the data distributions by the arriving time after PCAD classification. The results in Fig. 14 demonstrate that the points with surface scattering mainly distribute in 2–3.4 ns whereas the points with the other three types of scatterings are mainly in 3.4–4.3 ns. The

TABLE II
PCAD CLASSIFICATION RESULTS OF LANDMINE DATA

Candidate Targets	PCAD results (%)
Sphere (Surface scattering)	71.33
Cylinder (Dipole scattering)	18.31
Dihedral (Double-bounce scattering)	0.48
Multibranch scatterer (Volume scattering)	32.81

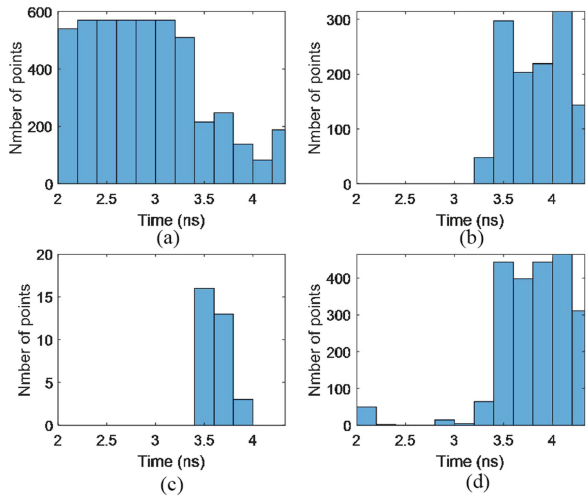

Fig. 14. Data distributions by the arriving time after PCAD classification. (a) Points with surface scattering. (b) Points with dipole scattering. (c) Points with double-bounce scattering. (d) Points with volume scattering.

distributions of different polarization components are consistent with the analytic results in Fig. 13.

Fig. 15(a) presents the FP-GPR radargrams extracted from the red rectangles in Fig. 12(c). Based on the PCAD classification results, we give the data points in this region with different colors and obtain a color-coded 2-D image in Fig. 15(b). Since the points with double-bounce scattering are far fewer than the points with other scatterings, they are excluded in the color-coded 2-D classification image. Besides, we merge the points with dipole and volume scatterings (marked with blue color) as they are both in region 2 and are much fewer than the points with surface scattering (marked with red color). The points with the mixture of three types of scatterings are marked with yellow color. Comparing the magnified radargrams with the color-coded 2-D image with PCAD classification results, we find that the points with surface scattering (red points) are coincident with the strong signals in HH and VV polarization radargrams and locate in the shallow part of the images, representing the signals from the surface of the landmine; the region with dipole and volume scatterings (blue points) are of the similar shape with the strong signals in HV polarization radargrams and distribute in the deep part of the images, representing the signals from the interior of the landmine. In general, the results are consistent with the analytic results in Fig. 13 and demonstrate that the landmine is a composite scatterer that can generate surface scattering signals on its surface and dipole and volume scattering signals from its interior. The results propose a new way to identify the landmine using the PCAD method.

V. DISCUSSION

A. Effects of the Particle Centers

In this section, we discuss the effects of the particle centers in targets identification. First, we test the traditional AdaBoost method without particle center processing. Fig. 16 presents two examples of computing the weak classifiers for the α parameter of the cylinder data (see the orange histogram in Fig. 16). Fig. 16(a) presents the result of the proposed PCAD method whereas Fig. 16(b) shows the result of the traditional AdaBoost method without particle center processing. The particle center processing can project the original data into a new domain where the target samples to be identified are concentrated close to 0. Therefore, in Fig. 15(a), only one weak classifier($r < 0.06$) is needed to identify the orange data and the error is less than 0.1. However, the target data in Fig. 16(b) is surrounded by the other data and two weak classifiers are needed to identify the orange histogram. The error curve 1 with red color is computed using (28), whereas the error curve 2 with blue color is computed using the following formula:

$$E_k'(r) = \frac{\sum_{n_1=1}^{N_1} \text{sign}\left(r - Z_{n_1}^1\right) + \sum_{t=2}^{4} \sum_{n_t=1}^{N_t} \text{sign}\left(Z_{n_t}^t - r\right)}{\sum_{t=1}^{4} N_t}. \tag{31}$$

The extreme points of the two error curves can determine the two weak classifiers (i.e., $r > 0.46$ and $r < 0.58$). However, the extreme points are not the minimums of the two error curves and are difficult to extract automatically. Besides, in Fig. 16(b), the error of the weak classifier 1 is approximately 0.3, which is much higher than the error in Fig. 16(a); the error of the weak classifier 2 is approximately 0.6, which is beyond 0.5 and is unusable according to the analysis in Section III-C. Therefore, particle center processing can reduce the number of weak classifiers and elevate their accuracy.

B. Comparison Between Particle Center and Traditional Average

We have analyzed that the particle center processing can map the original data into a new domain where the target samples to be identified are concentrated close to 0 and the weak classifier can be reduced to one. However, the mapping using the traditional average can also achieve the same goal so the comparison between the particle center and the traditional average is performed in this section. The procedure is similar to the proposed PCAD method in Section III-B and the only change is that the particle centers are replaced by the simple average of the data.

The identification accuracy of the single-parameter method and the average-based multiparameter method are also presented in Table I to compare with the results of the proposed method. The results show that both the single-parameter and multiparameter identification accuracy for the particle center-based method are higher than those of the average-based method, but the differences are not evident. Because the FP-GPR data used in the computations are collected in the laboratory environment,

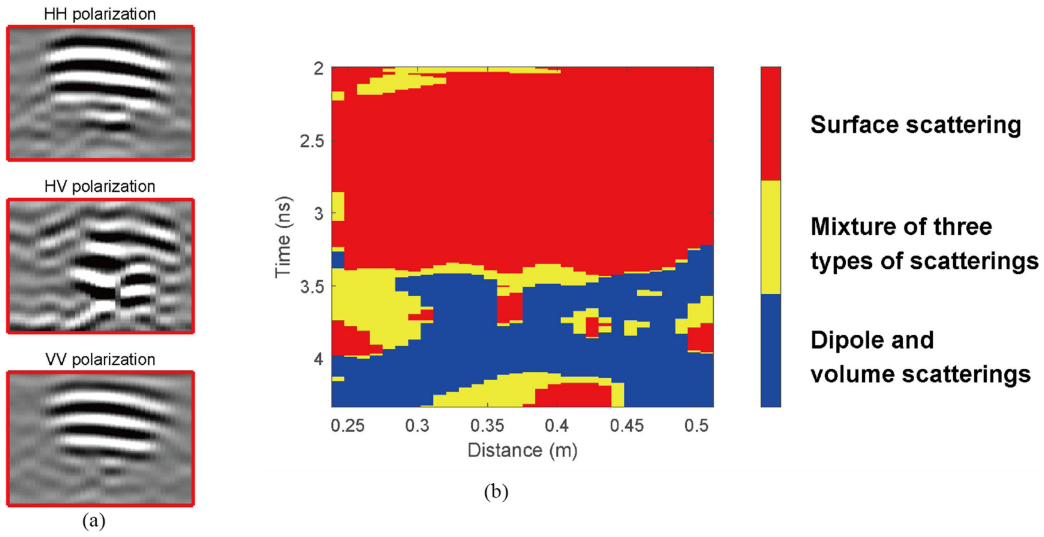

Fig. 15. Landmine identification results and analysis. (a) FP-GPR radargrams extracted from the red rectangles in Fig. 12(c). (b) Color-coded 2-D image with PCAD classification results.

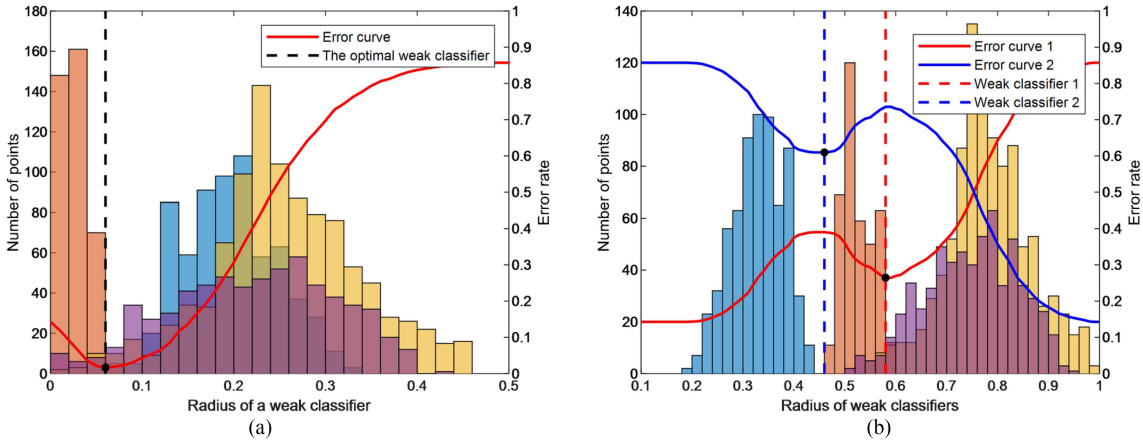

Fig. 16. Examples of the determination of weak classifiers for the α parameter of the cylinder data. (a) Result of the proposed PCAD method. (b) Result of the traditional AdaBoost method without particle center processing. The four color represent four datasets and the dataset with orange color is the cylinder data to be classified by the weak classifier.

the outliers in the data are few and their effects are not evident enough to present the advantages of the particle center. To illustrate, we simulate the cases with different effects of outliers and compute the averages and the particle centers of the data to compare their sensitivities to the outliers.

Firstly, a dataset Da_1 and an outlier dataset Da_2 are generated using the formula as follows:

$$\begin{cases} Da_1 = |\varepsilon_1 + \delta_1 \cdot randn(n_1)| \\ Da_2 = (\varepsilon_2 + d) + \delta_2 \cdot |randn(n_2)| \end{cases} \tag{32}$$

where randn$(\cdot)$ represents the Gaussian distribution function. Parameters $\varepsilon_{1,2}$, $\delta_{1,2}$, and $n_{1,2}$ denote the means, standard deviations, and the numbers of samples, respectively. We set $\varepsilon_1 = 0$, $\varepsilon_2 = 150$, $\delta_1 = 50$, $\delta_2 = 20$, $n_1 = 100$, and $n_2 = 20$. d is the variable parameter and is set to 1–200, which controls the distance between the normal dataset and the outlier dataset. The initial distributions of Da_1 and Da_2 are shown in Fig. 17(a). The blue and orange histograms represent the normal dataset and the outliers dataset, respectively. The normal data Da_1 concentrate between 0 and 50 and the outlier data Da_2 are close to Da_1. The parameter d varies from 1 to 200 and Fig. 17(b)–(f) presents the distributions of Da_1 and Da_2 when $d = 40$, 80, 120, 160, and 200, respectively. The distances between the normal data and the outliers data increase from (a) to (f). Simultaneously, the traditional averages and particle centers of the joint dataset of $Da1$ and $Da2$ are computed, which are presented in Fig. 18. The results demonstrate that when the distances between the normal data and outliers increase, the particle center will stay in the region that the normal data concentrate in whereas the traditional averages will move away from the region of normal data. Therefore, the traditional averages are much more sensitive to outliers. In this article, we choose to use the particle centers to perform the multiparameter target identifications. If the training data are of low quality, the proposed method can also reduce the effects of outliers and perform the identifications.

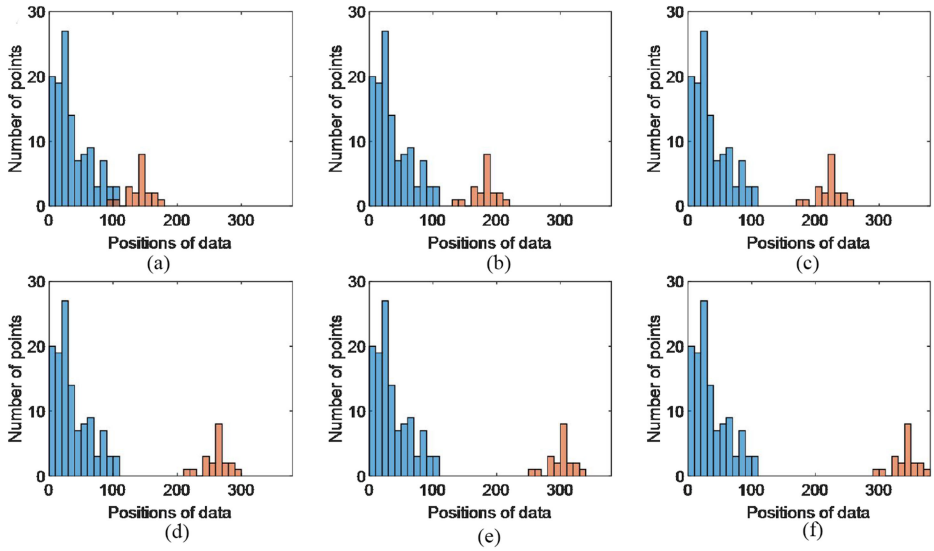

Fig. 17. Distributions of the data in the test of outliers. The blue and orange histograms represent the normal dataset and the outliers dataset, respectively. (a)–(f) Selected six cases when the parameter d varies from 1 to 200. (a)–(f) Correspond to $d = 1$, 40, 80, 120, 160, and 200, respectively. The distances between the normal dataset and the outliers dataset increase from (a) to (f).

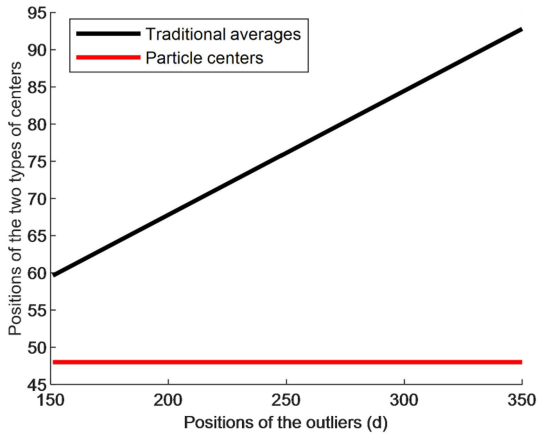

Fig. 18. Comparison of the sensitivity to the outliers between the particle centers and the traditional averages. When the outliers move away from the normal data, the traditional averages will change but the particle centers will stay.

C. Comparison With BAD Method

To illustrate the advancement of the proposed PCAD method, we compare it with the BAD method [31], which is also a modification of the traditional AdaBoost method. Fig. 19 compares the theories of the two methods. As Fig. 19(a) shows, the key of the BAD method is to sample with release from the initial dataset to generate a large number of subsets; subsequently, the AdaBoost procedures are performed for each subset to obtain a result; the final result is generated by the voting of the results from all the subsets. The method aims to reduce the impact of outliers by a large number of subsets.

We use the dataset in Section IV-A to test the BAD method. The BAD method usually uses a voting procedure to determine the final identification result and less abundant types of targets will be ignored. It means that the BAD method has a premise that the target to be classified should have only one type and it can not identify the composite target like a landmine. Therefore, this method can not obtain the subsurface distribution of different types of scatterings or the 2-D color-coded image generated in Section IV-C.

To make the results of the BAD method comparable with the proposed PCAD method, we use the average accuracy of all the subsets to represent the accuracy of the BAD method. In the test of the BAD method, there are two important parameters to specify, i.e., the number of subsets and the sampling rate, which are set to 1–1000 and 10–100%, respectively. Fig. 20 presents the relation between the number of subsets and the average accuracy when the sampling rate is set to 30%. The results demonstrate that when the scales of subsets are small (less than $\sim$300), the accuracy varies intensely; when the numbers of subsets exceed 300, the accuracy goes flat. Therefore, a large number of subsets are necessary to obtain relatively stable results. However, even the number of subsets reaches 1000, the accuracy of the BAD method is much lower than that of the PCAD method.

Fig. 21 illustrates the relationship between the sampling rate and the average accuracy when the number of subsets is set to 1000 in the BAD method. The results show no evident relationship between these two items so, for the BAD method, we may need to determine the best sampling rate through many times experiments.

Besides, Fig. 20 demonstrates that generating more large number of subsets can indeed enhance the stability and accuracy of the AdaBoost method but it can also make the computation more time-consuming. The running time of the BAD method and the proposed PCAD method are compared in Fig. 22, which indicates that the BAD method is more time-consuming with more subsets. If considering at least 300 subsets is necessary to obtain relatively stable results, the running time of the BAD method is more than five times that of the PCAD method. The details of the computation platform are shown in Table III.

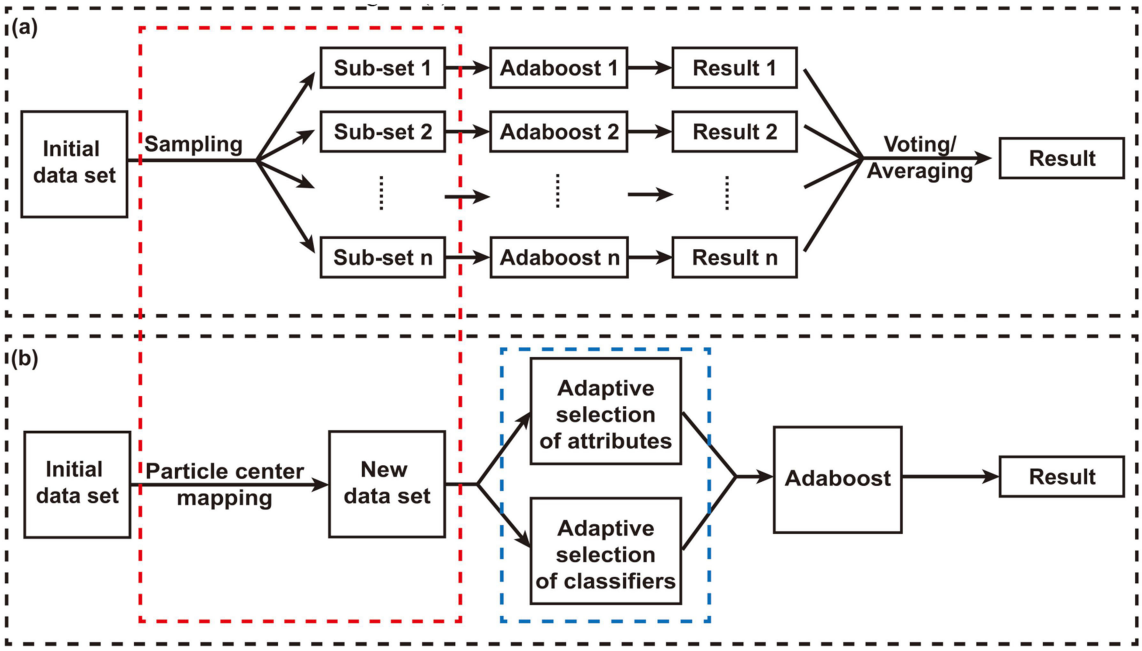

Fig. 19. Comparison between the BAD and the proposed PCAD methods. (a) Flowchart of the BAD method. (b) Flowchart of the proposed PCAD method.

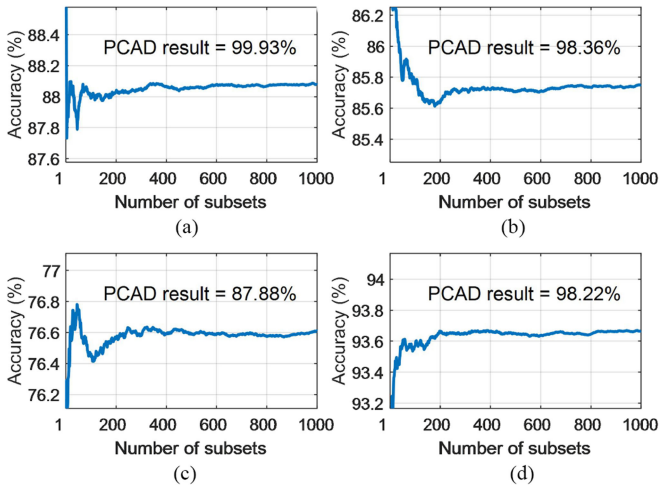

Fig. 20. Variations of average accuracy with the increasing number of subsets for four types of targets by the BAD method. The sampling rate in Bagging operation is set to 30%. (a) Metallic sphere. (b) Metallic cylinder. (c) Metallic dihedral. (d) Metallic multibranch.

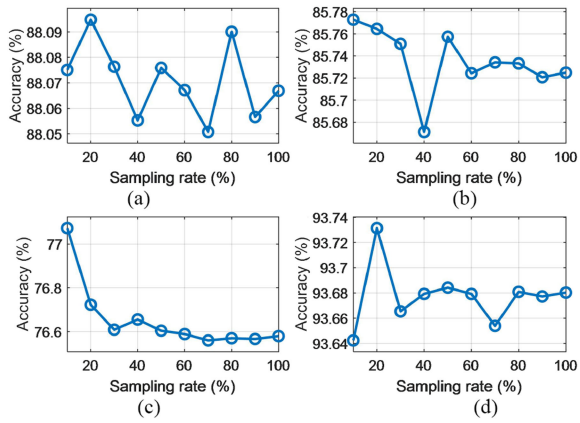

Fig. 21. Relationship between the average accuracy and the sampling rate in Bagging operation for four types of targets. The number of subsets is set to 1000. (a) Metallic sphere. (b) Metallic cylinder. (c) Metallic dihedral. (d) Metallic multibranch.

TABLE III
COMPUTATION PLATFORM

Terms	Details
System	Windows 10
CPU	AMD Ryzen 5 3600 6-Core Processor
CPU Clock Speed	3.6GHz
RAM	16 GB
Software	Matlab R2018a

The proposed PCAD method needs less running time because the procedure is more simple. As Fig. 19 shows, it only uses the particle center mapping to generate one new dataset rather than a large number of subsets in the BAD method. The aims of the operations in the red rectangle in Fig. 19 are similar, which are to reduce the impact of outliers. Essentially, the sampling operation in the Bagging method can also be seen as the searching of the sample center, but this method does not know, which data are the outlier, so it need to randomly generate a large number of subsets to determine the positions of outliers and reduce their interference by the voting operation.

On the contrary, the PCAD method can accurately locate the position of the main body of the data using the inversion method and subsequently exclude the interference of outliers. Besides, as the blue rectangle in Fig. 19 shows, the particle center mapping simultaneously achieves the adaptive selection of attributes and weak classifiers, which is beyond the ability of the previous BAD method.

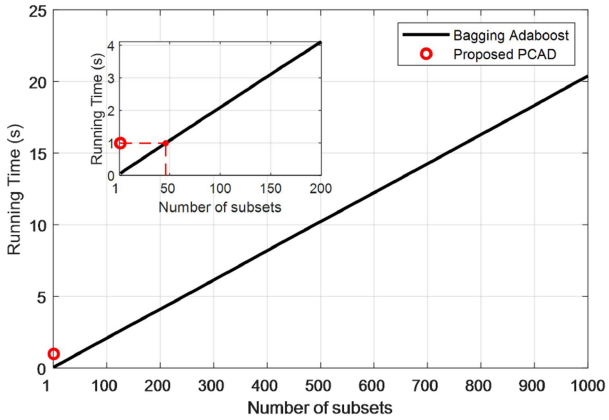

Fig. 22. Comparison of running time for the BAD and the proposed PCAD method.

In general, compared to the BAD method, the proposed PCAD method has the following advantages.

1) PCAD method can identify the composition of a complex target whereas the BAD method can not achieve this goal.
2) PCAD method has higher accuracy than the BAD method.
3) The BAD method has two important parameters to test and specify whereas the PCAD method has no parameter to set up.
4) To obtain relatively more stable results, the BAD method will cost several times of running time than that of PCAD method.
5) PCAD can directly suppress the interference of outliers by one-time inversion whereas the BAD method need to generate a large number of subsets to achieve the same goal.
6) PCAD method can simultaneously achieve the adaptive selection of attributes and weak classifiers, which is beyond the ability of the BAD method.

VI. Conclusion

In this article, we propose a PCAD method and achieve the multiparameter adaptive target identification of FP-GPR. The FP-GPR data of four types of targets are obtained and used for the training of the PCAD classifier. The experimental results demonstrate that the PCAD method can automatically select suitable parameters during the training process for different targets; compared to the single-parameter classification, the correct rates of the classification for the four targets are improved by PCAD. Further analysis verified the superiority of PCAD to the AdaBoost method based on the traditional average when dealing with outliers. When compared to the classic BAD method, the PCAD method is more advanced. In the application part, the proposed method is applied to the landmine detection and the color-coded 2-D image by PCAD is obtained for identification. The results demonstrate that the FP-GPR signals from the landmine contain different scattering modes, which are with different arrival time; the surface of the landmine can produce the surface scattering signals whereas its complex internal structure can generate approximately equal amounts of dipole and volume scattering signals. Based on these features, we can distinguish landmines from other targets.

References

[1] X. Feng and M. Sato, "Pre-stack migration applied to GPR for landmine detection," *Inv. Probl.*, vol. 20, no. 6, pp. S99–S115, Dec. 2004.
[2] E. Fisher, G. A. Mcmechan, A. P. Annan, and S. W. Cosway, "Examples of reverse-time migration of single-channel, ground-penetrating radar profiles," *Geophysics*, vol. 57, no. 4, pp. 577–586, Apr. 1992.
[3] X. Xu, E. L. Miller, and C. M. Rappaport, "Minimum entropy regularization in frequency-wavenumber migration to localize subsurface objects," *IEEE Trans. Geosci. Remote Sens.*, vol. 41, no. 8, pp. 1804–1812, Aug. 2003.
[4] X. Feng, Y. Yu, C. Liu, and M. Fehler, "Combination of H-Alpha decomposition and migration for enhancing subsurface target classification of GPR," *IEEE Trans. Geosci. Remote Sens.*, vol. 53, no. 9, pp. 4852–4861, Sep. 2015.
[5] X. Feng, W. Liang, C. Liu, E. Nilot, M. Zhang, and S. Liang, "Application of freeman decomposition to full polarimetric GPR for improving subsurface target classification," *Signal Process.*, vol. 132, pp. 284–292, Mar. 2017.
[6] X. Feng, Y. Yu, C. Liu, and M. Fehler, "Subsurface polarimetric migration imaging for full polarimetric ground-penetrating radar," *Geophys. J. Int.*, vol. 202, no. 2, pp. 1324–1338, Aug. 2015.
[7] Z. Dong, X. Feng, H. Zhou, C. Liu, and M. Sato, "Effects of induced field rotation from rough surface on H-alpha decomposition of full-polarimetric GPR," *IEEE Trans. Geosci. Remote Sens.*, vol. 59, no. 11, pp. 9192–9208, Nov. 2021.
[8] Z. Dong, X. Feng, H. Zhou, C. Liu, Qi Lu, and W. Liang, "Assessing the effects of induced field rotation on water ice detection of Tianwen-1 full-polarimetric mars rover penetrating radar," *IEEE Trans. Geosci. Remote Sens.*, vol. 60, 2021, Art. no. 4507313, doi: 10.1109/TGRS.2021.3138463.
[9] T. Miwa, M. Sato, and H. Niitsuma, "Subsurface fracture measurement with polarimetric borehole radar," *IEEE Trans. Geosci. Remote Sens.*, vol. 37, no. 2, pp. 828–837, Mar. 1999.
[10] J. Zhao and M. Sato, "Radar polarimetry analysis applied to singleholefully polarimetric borehole radar," *IEEE Trans. Geosci. Remote Sens.*, vol. 44, no. 12, pp. 3547–3554, Dec. 2006.
[11] G. P. Tsoflias, J. P. VanGestel, P. L. Stoffa, D. D. Blankenship, and M. Sen, "Vertical fracture detection by exploiting the polarization properties of ground-penetrating radar signals," *Geophysics*, vol. 69, no. 3, pp. 803–810, May 2004, doi: 10.1190/1.1759466.
[12] G. P. Tsoflias and A. Hoch, "Investigating multi-polarization GPR wave transmission through thin layers: Implications for vertical fracture characterization," *Geophys. Res. Lett.*, vol. 33, no. 20, pp. L20401, Oct. 2006, doi: 10. 1029/2006GL027788.
[13] D. S. Sassen and M. E. Everett, "3D polarimetric GPR coherency attributes and full-waveform inversion of transmission data for characterizing fractured rock," *Geophysics*, vol. 74, no. 3, pp. J23–J34, May 2009.
[14] C. C. Chen, M. B. Higgins, K. O'Neill, and R. Detsch, "Ultrawide-bandwidth fully-polarimetric ground penetrating radar classification of subsurface unexploded ordnance," *IEEE Trans. Geosci. Remote Sens.*, vol. 39, no. 6, pp. 1221–1230, Jun. 2001.
[15] K. O'Neill, "Discrimination of UXO in soil using broadband polarimetric GPR backscatter," *IEEE Trans. Geosci. Remote Sens.*, vol. 39, no. 2, pp. 356–367, Feb. 2001.
[16] F. Roth, P. van Genderen, and M. Verhaegen, "Processing and analysis of polarimetric ground penetrating radar landmine signatures," in *Proc. 2nd Int. Workshop Adv. GPR*, Delft, The Netherlands, 2003, pp. 70–75.
[17] I. L. Morrow and P. van Genderen, "A 2-D polarimetric backpropagation algorithm for ground-penetrating radar applications," *Microw. Opt. Technol. Lett.*, vol. 28, no. 1, pp. 1–4, Jan. 2001.
[18] K. O'Neill, S. A. Haider, S. D. Geimer, and K. D. Paulsen, "Effects of the ground surface on polarimetric features of broadband radar scattering from subsurface metallic objects," *IEEE Trans. Geosci. Remote Sens.*, vol. 39, no. 7, pp. 1556–1565, Jul. 2001.
[19] U. Boniger and J. Tronicke, "Subsurface utility extraction and characterization: Combining GPR symmetry and polarization attributes," *IEEE Trans. Geosci. Remote Sens.*, vol. 50, no. 3, pp. 736–746, Mar. 2012.
[20] B. J. Allred, J. J. Daniels, N. R. Fausey, C. C. Chen, L. Peters Jr, and H. S. Youn, "Important considerations for locating buried agricultural drainage pipe using ground penetrating radar," *J. Appl. Eng. Agriculture*, vol. 21, no. 1, pp. 71–87, Jan. 2005.
[21] S. R. Cloude and E. Pottier, "A review of target decomposition theorems in radar polarimetry," *IEEE Trans. Geosci. Remote Sens.*, vol. 34, no. 2, pp. 498–518, Mar. 1996.

[22] J. Zhao and M. Sato, "Consistency analysis of subsurface fracture characterization using different polarimetry techniques by a borehole radar," *IEEE Geosci. Remote Sens. Lett.*, vol. 4, no. 3, pp. 359–363, Jul. 2007.
[23] S. R. Cloude and E. Pottier, "An entropy based classification scheme for land applications of polarimetric SAR," *IEEE Trans. Geosci. Remote Sens.*, vol. 35, no. 1, pp. 68–78, Jan. 1997.
[24] J. S. Lee, M. R. Grunes, T. L. Ainsworth, L. J. Du, D. L. Schuler, and S. R. Cloude, "Unsupervised classification using polarimetric decomposition and the complex wishart classifier," *IEEE Trans. Geosci. Remote Sens.*, vol. 37, no. 5, pp. 2249–2258, Sep. 1999.
[25] A. Freeman and S L. Durden, "A three-component scattering model for polarimetric SAR data," *IEEE Trans. Geosci. Remote Sens.*, vol. 36, no. 3, pp. 963–973, May 1998.
[26] Q. Chen, Y. Jiang, L. Zhao, and G. Kuang, "Polarimetric scattering similarity between a random scatterer and a canonical scatterer," *IEEE Geosci. Remote Sens. Lett.*, vol. 7, no. 4, pp. 866–869, Oct. 2010.
[27] Q. Chen, G. Kuang, J. Li, L. Sui, and L. D., "Unsupervised land cover/land use classification using PolSAR imagery based on scattering similarity," *IEEE Trans. Geosci. Remote Sens.*, vol. 51, no. 3, pp. 1817–1825, Mar. 2013.
[28] X. Feng *et al.*, "Particle center supported plane for subsurface target classification based on full polarimetric ground penetrating radar," *Remote Sens.*, vol. 11, no. 4, pp. 405, Feb. 2019.
[29] Y. Freund and R. E. Schapire, "A decision-theoretic generalization of on-line learning and an application to boosting," *J. Comput. Syst. Sci.*, vol. 55, no. 1, pp. 119–139, 1995.
[30] A. Krogh and J. Vedelsby, "Neural network ensembles, cross validation and active learning," *Adv. Neural Inf. Process. Syst.*, vol. 7, no. 10, pp. 231–238, Jan. 1994.
[31] L. Breiman, "Bagging predictors," *Mach. Learn.*, vol. 24, no. 2, pp. 123–140, Aug. 1996.
[32] L. Breiman, "Random forests," *Mach. Learn.*, vol. 45, no. 1, pp. 5–32, Oct. 2001.
[33] R. Bryll, R. Gutierrez-Osuna, and F. Quek, "Attribute bagging: Improve accuracy of classifier ensembles by using random feature subsets," *Pattern Recognit.*, vol. 36, no. 6, pp. 1291–1302, Jun. 2003.
[34] Z. Zhou, J. Wu, and W. Tang, "Combining regression estimators: GA-based selective neural network ensemble," *Int. J. Comput. Int. Appl.*, vol. 1, no. 4, pp. 341–356, 2001.
[35] J. Kennedy and R. Eberhart, "Particle swarm optimization," in *Proc. Int. Conf. Neural Netw.*, 1995, pp. 1942–1948.
[36] H. Zhou*et al.*, "Combination of support vector machine and H-alpha decomposition for subsurface target classification of GPR," in *Proc. IEEE Int. Conf. Ground Penetrating Radar*, 2018, pp. 635–638.
[37] H. Liu, J. Zhong, F. Ding, X. Meng, C. Liu, and J. Cui, "Detection of early-stage rebar corrosion using a polarimetric ground penetrating radar system," *Construction Building Mater.*, vol. 317, no. 24, pp. 1–10, Jan. 2022.
[38] H. Zhou, X. Feng, Z. Dong, C. Liu, W. Liang, and Y. An, "Local freeman decomposition for robust imaging and identification of subsurface anomalies using misaligned full-polarimetric GPR data," *Remote Sens.*, vol. 14, no. 3, Feb. 2022, Art. no. 804.

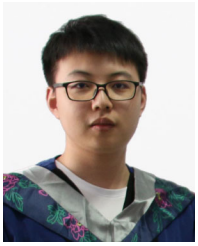

Haoqiu Zhou (Student Member, IEEE) received the B.S. and M.S. degrees in geophysics of solid earth in 2017 and 2020, respectively, from Jilin University, Changchun, China, where he is currently working toward the Ph.D. degree in solid earth geophysics with the College of Geo-Exploration Science and Technology.

His research interests include signal processing and analysis of ground penetrating radar and machine learning technology.

Xuan Feng (Senior Member, IEEE) received the B.S. degree in applied geophysics and the M.S. and Ph.D. degrees in geo-exploration and information technology from Jilin University, Changchun, China, in 1996, 1999, and 2002, respectively.

From 2003 to 2005, he held a Postdoctoral Position, and, from 2005 to 2006, he was a Research Assistant with Tohoku University, Sendai, Japan, respectively. From 2006 to 2008, he was an Associate Professor with Jilin University, Changchun, China. From 2014 to 2016, he was a visiting scientist with MIT. Since 2008, he has been a Professor with Jilin University and has been the Deputy Dean of College of Geo-exploration Science and Technology since 2017. His research interests include signal processing technology of ground penetrating radar and seismic exploration, and joint inversion of GPR and seismic exploration.

Zejun Dong received the B.S. and M.S. degrees in geophysics of solid earth in 2016 and 2019, respectively, from Jilin University, Changchun, China, where she is currently working toward the Ph.D. degree in solid earth geophysics with the College of Geo-Exploration Science and Technology.

In 2018, she was an exchange student with Tohoku University, Sendai, Japan. Her research interests include numerical simulation and signal processing and analysis of ground penetrating radar.

Cai Liu received the B.S. degree in applied geophysics and the M.S. and Ph.D. degrees in geo-exploration and information technology from Jilin University, Changchun, China, in 1986, 1993, and 1999, respectively.

From 1996 to 2000, he was an Associate Professor with Jilin University, Changchun, China, became a Professor in 2000, and Distinguished Professor of Jilin Province, China, in 2008. He was the Director with the College of Geo-Exploration Science and Technology, Jilin University from 2004 to 2017. He is in the Ten Thousand Talent Program since 2018. His research interests include the integrated research of geophysics and geology.

Wenjing Liang received the B.S., M.S., and Ph.D. degrees in geophysics of solid earth from Jilin University, Changchun, China, in 2009, 2012, and 2018, respectively.

She is currently with the College of Geo-Exploration Science and Technology, Jilin University. Her research interests include GPR system and signal processing.